

# Amorphous Redox-Rich Polysulfides for Mg Cathodes

Minglei Mao, Chenxing Yang, Zejing Lin, Yuxin Tong, Qinghua Zhang, Lin Gu, Liang Hong, Liumin Suo,\* Yong-Sheng Hu, Hong Li, Xuejie Huang, and Liquan Chen

Cite This: <https://doi.org/10.1021/jacsau.1c00144>

Read Online

ACCESS |

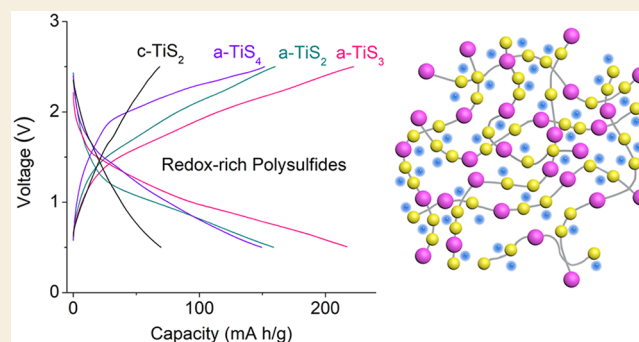
Metrics & More

Article Recommendations

Supporting Information

**ABSTRACT:** The lack of appropriate cathodes is restraining the advances of Mg batteries. Crystalline cathode materials suffer from sluggish reaction kinetics and low-capacity delivery. The finite type of crystalline structure further confines the rational design of cathode materials. Herein, we proposed amorphization and anion enrichment as a brand-new strategy to not only enhance the solid-state ion diffusion and provide more ion-storage sites in amorphous structure but also contribute to the local transfer of multiple electrons through the additional anionic redox centers. Accordingly, a series of amorphous titanium polysulfides ( $a\text{-TiS}_x$ ,  $x = 2, 3, \text{ and } 4$ ) were designed, which significantly outperformed their crystalline counterparts and achieved a highly competitive energy density of  $\sim 260$  Wh/kg. The unique  $\text{Mg}^{2+}$  storage mechanism involves the dissociation/formation of S–S bonds and changes in the coordination number of Ti, namely, a mixture of conversion and intercalation reaction, accompanied by the joint cationic (Ti) and anionic (S) redox-rich chemistry. Our proposed amorphous and redox-rich design philosophy might provide an innovative direction for developing high-performance cathode materials for multivalent-ion batteries.

**KEYWORDS:** Mg battery, cathode, amorphous, titanium polysulfides, joint cationic and anionic redox chemistry, mixture of conversion and intercalation reaction



## INTRODUCTION

Rechargeable Mg batteries (RMBs) are attracting more research focus in the postlithium era, because of several merits of Mg anodes: high abundance, high capacity (2205 mA h/g and 3833 mA h/cm<sup>3</sup>), easy processing at ambient atmosphere, less prone to form dendrites, and high Coulombic efficiency for Mg stripping/deposition.<sup>1–3</sup> However, the development of RMBs is severely afflicted by a lack of appropriate cathodes. Crystalline oxide cathode materials are excluded by sluggish reaction kinetics and low magnesian degree, resulting from strong electrostatic interactions between highly polarized  $\text{Mg}^{2+}$  and host lattices.<sup>4–6</sup> Moreover, magnesium thermodynamically tends to abstract oxygen from the lattice to form the MgO-containing amorphous interface,<sup>7,8</sup> which will prohibit the electrochemical reaction from penetrating deeply into the bulk phase. Regarding crystalline sulfide cathode materials, though moderate success has been realized,<sup>9–11</sup> their implementation is hindered by low-capacity delivery.<sup>10–12</sup>

When  $\text{Mg}^{2+}$  with high charge density is intercalated into the crystalline structure, the surrounding electrostatic field of the host lattice changes dramatically, leading to high diffusion energy barriers of  $\text{Mg}^{2+}$ .<sup>4</sup> In addition, the single-electron transfer of traditional cationic redox chemistry further delays the local charge-compensation process, contributing to the sluggish diffusion kinetics of  $\text{Mg}^{2+}$ .<sup>13</sup> Worse still, upon massive

electron injection brought by  $\text{Mg}^{2+}$  insertion, unstable lattice distortions and irreversible structural collapse tends to happen, further resulting in the failure and poor reversibility of the materials (Figure 1a). Therefore, the design of  $\text{Mg}^{2+}$  hosts should focus on an open and random structure with rich active sites and good charge-compensation ability.

Amorphization is proposed to break out of the confinement of the crystalline structure. First, amorphization can potentially provide extra capacities, due to the presence of additional stable sites for magnesium ions on the basis of an open and random structure in amorphous materials (Figure 1b). Second, structural flexibility and free volume resulting from amorphization might contribute to the insertion kinetics of highly polarized  $\text{Mg}^{2+}$ .<sup>14</sup> Third, amorphization may enhance reversibility by providing a network capable of absorbing considerable deformations caused by magnesium insertion.<sup>15</sup> Lastly, amorphization can freely tune the composition of compounds

Received: March 31, 2021

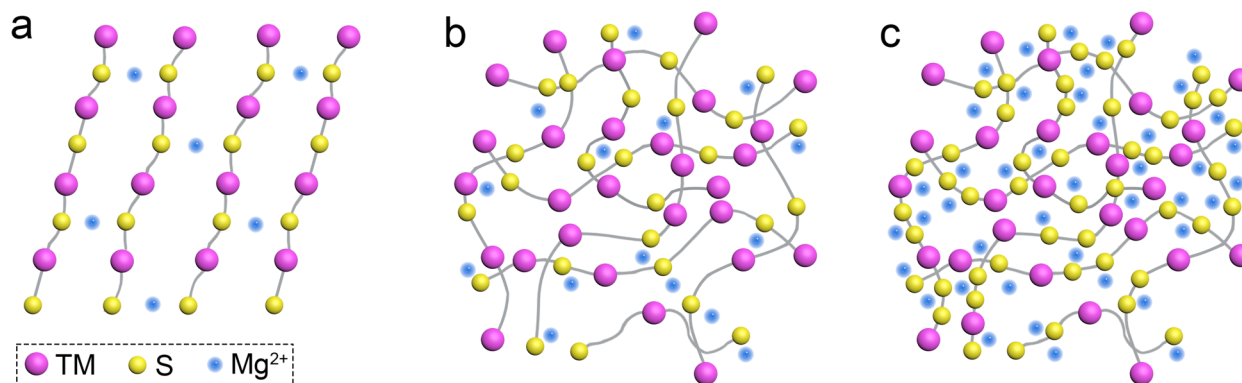


**Figure 1.** Design principle of amorphous and redox-rich polysulfides for Mg batteries.  $\text{Mg}^{2+}$  insertion into (a) crystalline transition metal (TM) sulfides, (b) amorphous TM sulfides, and (c) amorphous TM polysulfides.

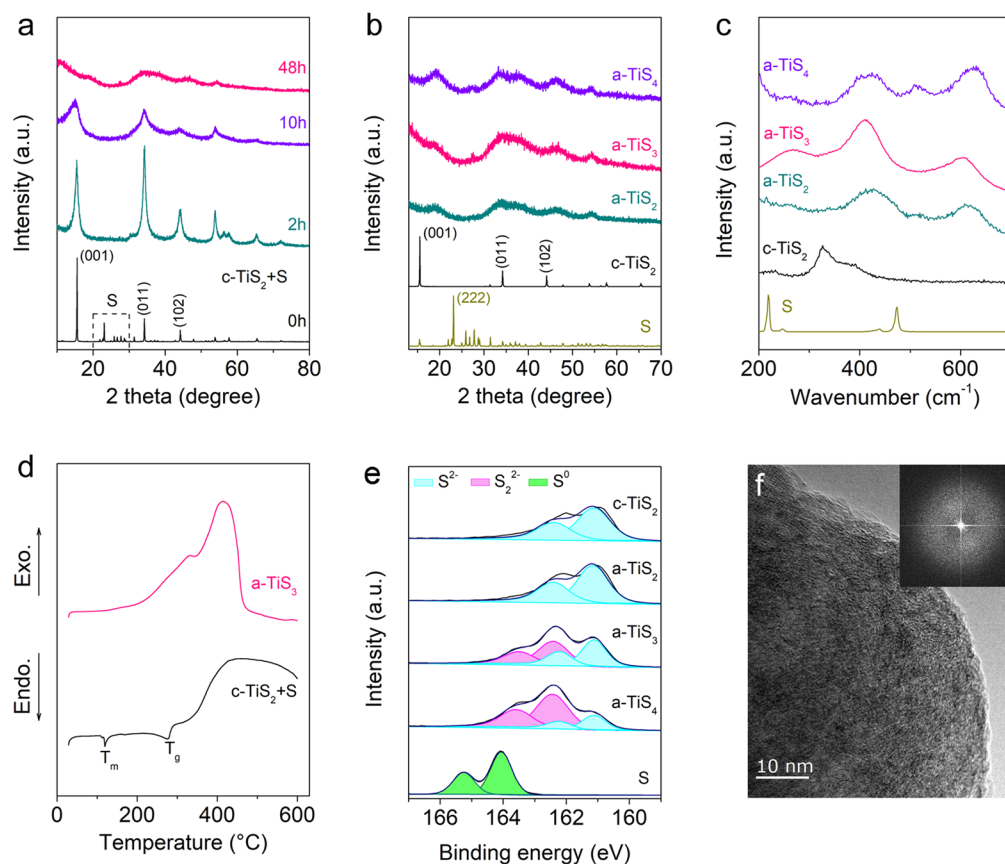


**Figure 2.** Characterizations of  $\text{a-TiS}_x$  samples ( $x = 2, 3,$  and  $4$ ). (a) XRD patterns of  $\text{c-TiS}_2 + \text{S}$  mixture with various ball-milling durations from 0 to 48 h. (b) XRD patterns and (c) Raman spectra of sulfur,  $\text{c-TiS}_2$ , and  $\text{a-TiS}_x$  samples. (d) DSC of  $\text{a-TiS}_3$  and  $\text{c-TiS}_2 + \text{S}$  samples. (e) XPS S 2p of S,  $\text{c-TiS}_2$ , and  $\text{a-TiS}_x$  samples. Light blue, pink, and green represent  $\text{S}_2^{2-}$ ,  $\text{S}^{2-}$ , and  $\text{S}^0$ , respectively. (f) TEM images of  $\text{a-TiS}_3$  samples. Inset is the FFT.

(Figure 1c). For sulfide materials, amorphization can vary the sulfur content to result in a more oxidized state of sulfur ligands than  $\text{S}^{2-}$ ,<sup>16–21</sup> which will instigate redox-rich chemistry (joint cationic and anionic redox chemistry) and enhance the capacity delivery.

Herein, we designed a series of amorphous titanium polysulfides ( $\text{a-TiS}_x$ ,  $x = 2, 3,$  and  $4$ ) as cathode materials in multivalent ion batteries. The amorphous sulfides significantly outperformed their corresponding crystalline sulfides. The magnesiation/demagnesiation process was demonstrated to involve the dissociation/formation of S–S bonds and changes in the coordination number of Ti. The valence change was

extensively studied, in which both cationic titanium and anionic sulfur are redox-active.

## RESULTS AND DISCUSSION

The crystallinity evolution of the  $\text{c-TiS}_2 + \text{S}$  mixture with ball-milling time was investigated by X-ray diffraction (XRD; Figure 2a). The diffraction peaks assigned to sulfur disappear after 2 h of ball-milling, while the intensity attributable to  $\text{c-TiS}_2$  peaks gradually fades over the milling time. A halo pattern is dominant after 48 h, indicating that the pristine crystalline  $\text{c-TiS}_2 + \text{S}$  mixture is completely converted into amorphous states. Similarly, a series of amorphous  $\text{TiS}_x$  ( $x = 2, 3,$  and  $4$ )

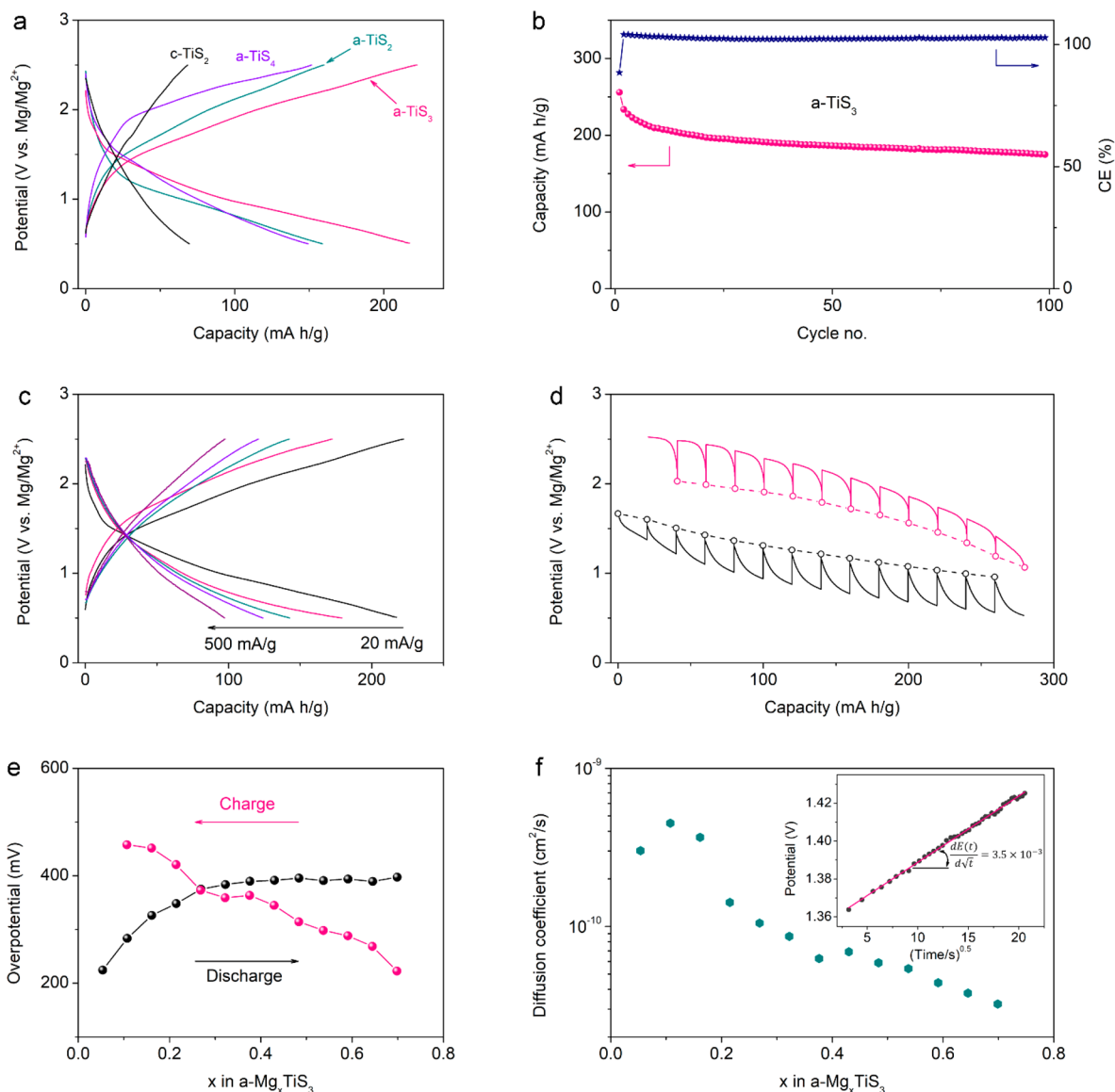


**Figure 3.** Electrochemical performance of a-TiS<sub>x</sub> samples using pouch cells with the MACC electrolyte and metallic Mg anode between 0.5 and 2.5 V at 60 °C. (a) Typical discharge/charge curves at 20 mA/g. (b) Cycling performance of a-TiS<sub>3</sub> sample for the first 100 cycles at 20 mA/g. (c) Current density dependence of the discharge/charge curves of a-TiS<sub>3</sub>/Mg pouch cells. (d) Quasi-equilibrium voltage profile of a-TiS<sub>3</sub>/Mg pouch cells obtained from galvanostatic intermittent titration technique (GITT) measurements. The cells were allowed to relax for 2 h after every 1 h of discharging or charging at 20 mA/g. The open circles represent the equilibrium open-circuit potentials. (e) Absolute value of the voltage difference for the system with the current on and after 2 h relaxation for the discharging and charging process. (f) Mg<sup>2+</sup> diffusion coefficients determined by GITT. Inset is the representation of the transient voltage of the galvanostatic pulse as a function of the square root of the time for a-TiS<sub>3</sub> sample. The red dashed line is the linear fitting, and the slope of the linear fitting is presented in the plot.

(a-TiS<sub>x</sub>) samples were obtained after 48 h of ball-milling (Figure 2b). Raman spectroscopy, differential scanning calorimetry (DSC), X-ray photoelectron spectroscopy (XPS), and transmission electron microscopy (TEM) were further conducted to consolidate amorphous states of a-TiS<sub>x</sub> (Figure 2c–f). The typical Raman peaks for sulfur (218.8 and 473.6 cm<sup>-1</sup>)<sup>22</sup> and c-TiS<sub>2</sub> (327.2 cm<sup>-1</sup>)<sup>23</sup> completely disappear in a-TiS<sub>x</sub> samples, while three new peaks at 427.8, 514.5, and 628.4 cm<sup>-1</sup> emerge (Figure 2c). Two DSC endothermic peaks of the TiS<sub>2</sub> + S mixture at 119 and 280 °C represent the melt ( $T_m$ ) and gasification ( $T_g$ ) of sulfur, both of which vanish for the a-TiS<sub>3</sub> sample (Figure 2d), indicative of the formation of a new bond between pristine S and TiS<sub>2</sub>. The XPS S 2p spectra of both c-TiS<sub>2</sub> and a-TiS<sub>2</sub> are composed of two sets of doublet

peaks, corresponding to S 2p<sub>3/2</sub> and S 2p<sub>1/2</sub> of S<sup>2-</sup>. While for a-TiS<sub>3</sub> and a-TiS<sub>4</sub> samples, two new sets of doublet peaks ascribed to S 2p<sub>3/2</sub> and S 2p<sub>1/2</sub> of S<sub>2</sub><sup>2-</sup> appear, indicating that amorphization by ball-milling enables the formation of titanium polysulfides. No S 2p peaks of a-TiS<sub>3</sub> and a-TiS<sub>4</sub> samples can be assigned to S<sup>0</sup>, indicating that all the sulfur is bonded with titanium in the a-TiS<sub>x</sub> samples (Figure 2e). The particle sizes of a-TiS<sub>x</sub> samples are substantially reduced to the nanoscale by the ball-milling process (Figures S1–S7). The titanium and sulfur signals in energy-dispersive spectroscopy (EDS) mapping images well overlap (Figure S6), suggesting that Ti and sulfur are not separately present. The TEM image of the a-TiS<sub>3</sub> sample shows no periodic lattice fringes, corresponding to a halo pattern in the fast Fourier transform

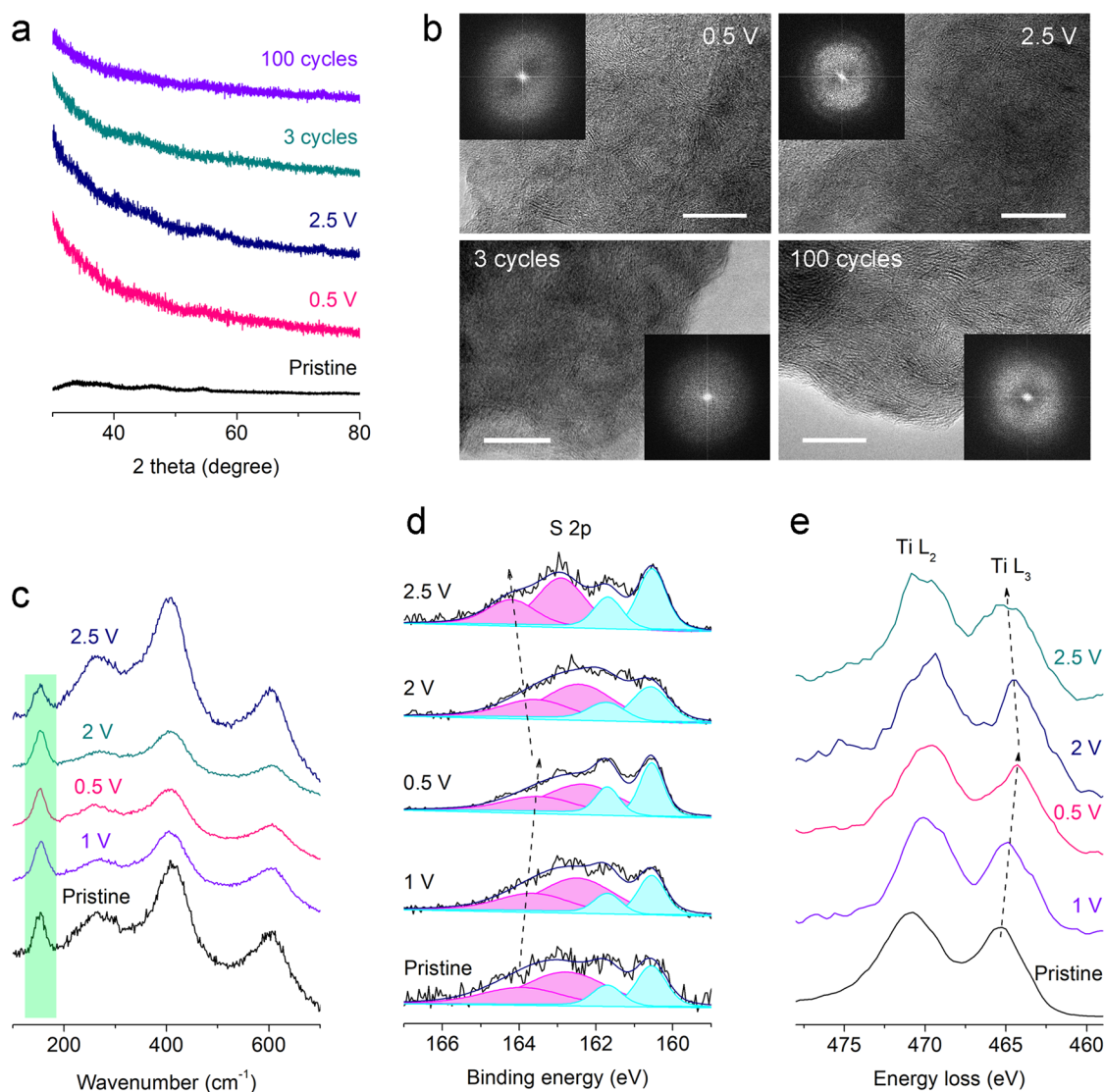


**Figure 4.** Reaction mechanism of a-TiS<sub>3</sub> sample during cycling. Ex situ (a) XRD and (b) high-resolution TEM (HRTEM) of the a-TiS<sub>3</sub> sample at various states: pristine, fully discharged to 0.5 V, fully recharged to 2.5 V, after 3 cycles, and after 100 cycles. Inset is the corresponding FFT. Scale bar: 10 nm. Ex situ (c) Raman spectra, (d) XPS S 2p, and (e) EELS Ti-L of the a-TiS<sub>3</sub> sample at various states: pristine, discharged to 1 V, fully discharged to 0.5 V, recharged to 2 V, and fully recharged to 2.5 V.

(FFT) pattern (Figure 2f). All the characterizations corroborate the formation of amorphous a-TiS<sub>x</sub> samples.

The electrochemical performance of a-TiS<sub>x</sub> samples was evaluated using pouch cells with MACC electrolyte and a metallic Mg anode between 0.5 and 2.5 V (Figure 3). Compared to c-TiS<sub>2</sub>, a-TiS<sub>2</sub> delivers a much higher capacity of 160 mA h/g, indicating the better reaction kinetics of the a-TiS<sub>2</sub> sample (Figure 3a). Elevating the sulfur content to a-TiS<sub>3</sub>, a high capacity of 220 mA h/g is achieved, much higher than that of the c-TiS<sub>2</sub> + S mixture (Figure S13) and c-TiS<sub>3</sub> (Figures S11, 12, S14). Both the discharging and charging curves of a-TiS<sub>3</sub> exhibit a gradual slope for 1.25-electron-transfer processes, possibly corresponding to a gradual change in the structure of the amorphous host. Further increasing the sulfur content, the a-TiS<sub>4</sub> sample, however, has a lower capacity (150 mA h/g) than a-TiS<sub>3</sub> sample, probably due to the sharp drop of the electronic conductivity and thus sluggish reaction kinetics (Figure S15 and Table S1).<sup>4,17</sup> Therefore, the a-TiS<sub>3</sub> sample is targeted for detailed investigation. Despite a moderate decrease of capacity in the initial several cycles, the

a-TiS<sub>3</sub> sample exhibits an appreciable capacity retention of 80%, in which a high capacity of 175 mA h/g is maintained after 100 cycles (Figure 3b). The rate capability of the a-TiS<sub>3</sub> sample was also investigated, in which the capacities of 180 and 143 mA h/g are achieved at 50 and 100 mA/g, respectively (Figure 3c). Even at an ultrahigh current density of 500 mA/g, the a-TiS<sub>3</sub> sample still delivers a high capacity of 97 mA h/g, indicating respectable reaction kinetics.

To further decipher the reaction kinetics of a-TiS<sub>3</sub> sample, overpotentials from quasi-equilibrium states were collected using the galvanostatic intermittent titration technique (GITT) (Figure 3d–f). The cells were allowed to relax for 2 h at an open circuit to reach quasi-equilibrium after each 1 h discharging or charging period at 20 mA/g in the first cycle (Figure 3d). The cumulative capacities are 280 mA h/g on discharging and 259 mA h/g on charging, both of which are greater than those during the galvanostatic discharging/charging process. A slope line is obtained across the open circles accompanied by close hysteresis for various magnesia-tion degrees (Figure 3e), not typically characteristic of a phase

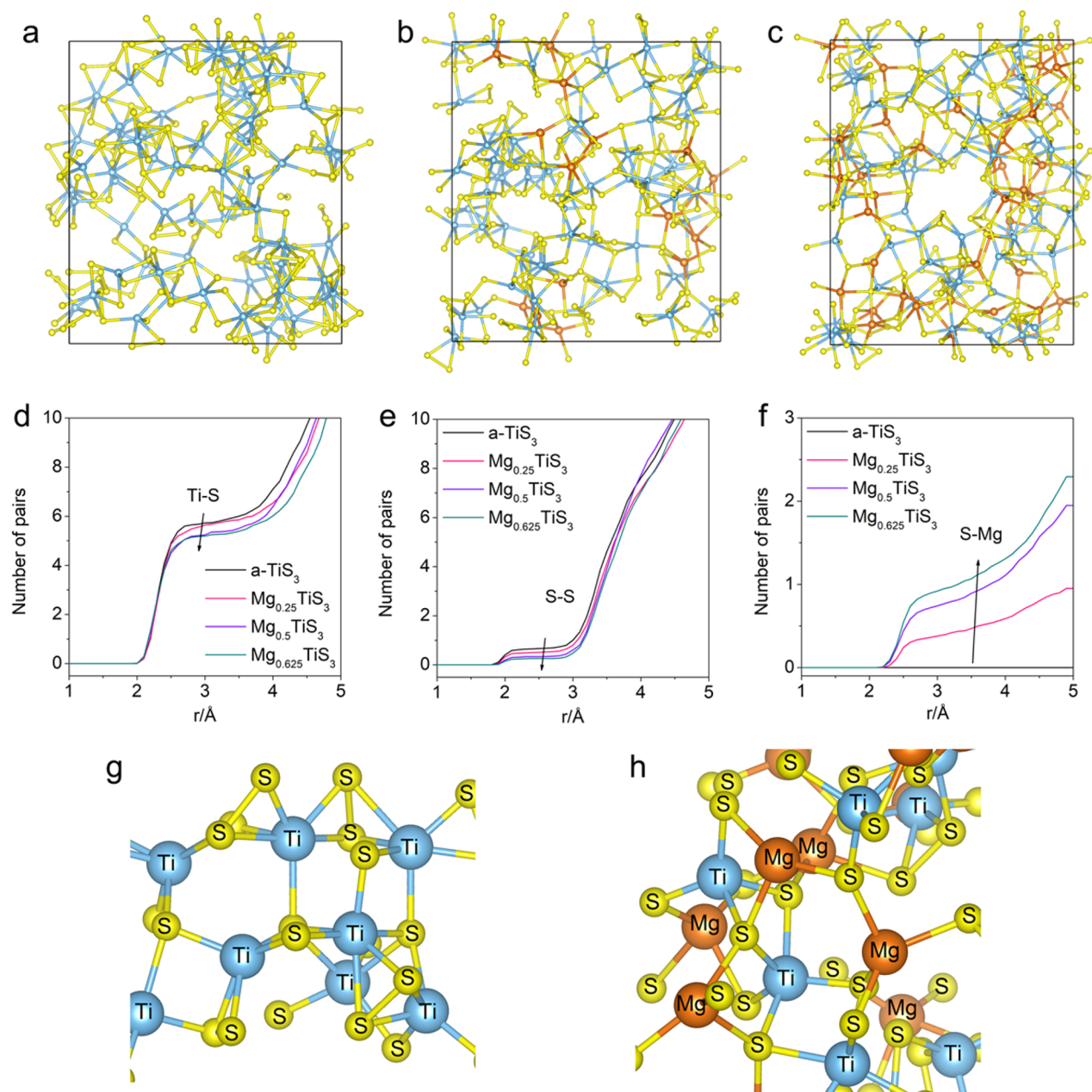


**Figure 5.** Investigation of the structure change of a-TiS<sub>3</sub> upon magnesion using DFT-MD simulation. Structure models of (a) a-TiS<sub>3</sub>, (b) a-Mg<sub>0.25</sub>TiS<sub>3</sub>, and (c) a-Mg<sub>0.625</sub>TiS<sub>3</sub>. Relationship between the number of pairs and distance, *r*, for (d) Ti–S, (e) S–S, and (f) S–Mg correlations derived from a-TiS<sub>3</sub>, a-Mg<sub>0.25</sub>TiS<sub>3</sub>, a-Mg<sub>0.5</sub>TiS<sub>3</sub>, and a-Mg<sub>0.625</sub>TiS<sub>3</sub> models. The number of first-neighbor Ti–S represents the average coordination number of Ti. Local structure models of (g) a-TiS<sub>3</sub> and (h) a-Mg<sub>0.625</sub>TiS<sub>3</sub>.

transformation reaction. No kinetics improvement in the demagnesion process indicates that the a-TiS<sub>3</sub> sample does not undergo a conversion reaction. Otherwise, the a-TiS<sub>3</sub>/Mg battery will be converted into a kind of Mg/S system, resulting in highly improved kinetics during charge.<sup>24</sup>

The chemical diffusion coefficient for Mg<sup>2+</sup> in a-TiS<sub>3</sub> at various magnesion degrees is obtained from GITT using eq 1.<sup>25–27</sup>

$$D = \frac{4}{\pi} \left( \frac{IV_M}{Z_A F S} \right)^2 \left[ \frac{dE(x)/dx}{dE(t)/d\sqrt{t}} \right]^2 \quad (1)$$

where *I* is the applied constant current, *V<sub>M</sub>* is the molar volume of a-TiS<sub>3</sub> (56.16 cm<sup>3</sup>/mol), assumed to be constant during the electrochemical process, *Z<sub>A</sub>* is the charge number of electro-

active species Mg<sup>2+</sup>, *F* is the Faraday constant (96 486 C/mol), *S* is the electrochemical active area between the a-TiS<sub>3</sub> sample and electrolyte from the Brunauer–Emmett–Teller (BET) surface area (*S<sub>BET</sub>* = 1.15 × 10<sup>5</sup> cm<sup>2</sup>/g) (Figure S20), *E*(*x*) is the steady-state equilibrium voltage (i.e., open circuit voltage) of the working electrode at the composition of a-Mg<sub>*x*</sub>TiS<sub>3</sub>, while *E*(*t*) is the transient voltage response of the a-TiS<sub>3</sub> electrode during the constant current interval. The transient voltage versus the square root of the time is plotted in the inset of Figure 3f. Plugging the slope of the linear fitting into eq 1, we can get the diffusion coefficient of Mg<sup>2+</sup> in the a-TiS<sub>3</sub> sample, varying from 3.2 × 10<sup>−11</sup> to 4.5 × 10<sup>−10</sup> cm<sup>2</sup>/s, indicating the highly competitive reaction kinetics of Mg<sup>2+</sup> in a-TiS<sub>3</sub> samples.<sup>4,10,12,19,26</sup>

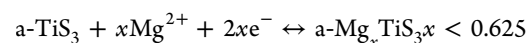
Ex situ XRD, TEM, Raman spectroscopy, XPS, and EELS were implemented to unveil the reaction mechanism of the a-TiS<sub>3</sub> sample (Figure 4). No crystalline peaks in XRD patterns can be observed at various states and after cycles (Figure 4a), indicating that the a-TiS<sub>3</sub> sample remains amorphous during cycling. HRTEM images show no periodic lattice fringes corresponding to the halo patterns of FFT (Figure 4b), further supporting amorphous states of the a-TiS<sub>3</sub> sample. The atomic ratios of S/Ti were also monitored at various states (Figure S21), in which the ratio remains ~3 even after 100 cycles. Negligible sulfur dissolution excludes the conversion reaction. Otherwise, the severe dissolution of polysulfide might cause much lower atomic ratios of S/Ti. Four prominent Raman peaks located at 600, 410, 260, and 155 cm<sup>-1</sup> remain present at various states without new peaks emerging (Figure 4c). The lowest-frequency peak (155 cm<sup>-1</sup>) originates from the out-of-phase rigid vibration of each 1D-like a-TiS<sub>3</sub> chain extending along the length of the chain,<sup>28,29</sup> which is expected to remain unchanged during cycling. Accordingly, the relative intensity of the other three peaks (600, 410, and 260 cm<sup>-1</sup>) constantly diminish due to the Mg<sup>2+</sup> uptake and progressively recover after Mg<sup>2+</sup> removal. The intensity of all the four peaks almost returns to the pristine one, indicating the highly reversible structure change of a-TiS<sub>3</sub> upon Mg<sup>2+</sup> insertion.

Ex situ XPS and EELS measurements were further performed to clarify the valence change of the a-TiS<sub>3</sub> sample during the discharge/charge process (Figures 4d,e and S23–S26). The S 2p spectra of a-TiS<sub>3</sub> are composed of two sets of doublet peaks (S 2p<sub>3/2</sub> and S 2p<sub>1/2</sub>). One set of doublet peaks located at 164.01 and 162.79 eV corresponds to 2p<sub>1/2</sub> and 2p<sub>3/2</sub> of S<sub>2</sub><sup>2-</sup>, while the others peaks at 161.71 and 160.56 eV correspond to 2p<sub>1/2</sub> and 2p<sub>3/2</sub> of S<sup>2-</sup>.<sup>30,31</sup> During the discharge process from pristine to 0.5 V, the 2p<sub>1/2</sub> peak of S<sub>2</sub><sup>2-</sup> shifts toward the lower binding energy (Figure 4d), indicating that Mg<sup>2+</sup> uptake causes the decrease of S<sub>2</sub><sup>2-</sup> valence. Upon recharging from 0.5 to 2.5 V, the peaks move back close to the pristine one, in accord with the results of ex situ EELS S-L spectra (Figure S26). The reversible shift of binding energy demonstrates that anionic sulfur takes part in the redox reaction. For XPS of Ti 2p, the typical binding energies of 462.9 and 456.8 eV represent Ti 2p<sub>1/2</sub> and Ti 2p<sub>3/2</sub>, respectively (Figure S23).<sup>32–34</sup> Similar to the evolution of S<sub>2</sub><sup>2-</sup> peaks, Ti 2p peaks gradually move to a lower binding energy upon discharge, followed by a shift back during the demagnesian process, signifying that cationic titanium involves the redox reaction. No peaks for elemental sulfur and titanium are observed,<sup>31</sup> indicating that the a-TiS<sub>3</sub>/Mg system does not experience a conversion reaction. The evolution of EELS Ti-L was also monitored (Figure 4e), in which Ti L<sub>3</sub> peaks progressively shift to lower energies throughout the discharge process, followed by the recovery to higher energies during the recharge process. The reversible shift of Ti L<sub>3</sub> peaks indicates that Ti involves the redox reaction during the discharge/charge process. Accordingly, upon Mg uptake and removal, both cationic Ti and S take part in the redox reaction, called joint cationic and anionic redox chemistry (CARC).

To unveil the structure change of a-TiS<sub>3</sub> during the magnesian process, an amorphous structure model was developed by melt quenching using density functional theory based molecular dynamics (DFT-MD) simulations (Figure 5). The structural models derived from the DFT-MD calculations are displayed in Figures 5a–c and S19. Figure 5d–f exhibits

the relationship between the number of pairs and the distance, *r*, for the Ti–S, S–S, and S–Mg correlations, respectively. The average coordination numbers of Ti for a-TiS<sub>3</sub>, a-Mg<sub>0.25</sub>TiS<sub>3</sub>, a-Mg<sub>0.5</sub>TiS<sub>3</sub>, and a-Mg<sub>0.625</sub>TiS<sub>3</sub> are ca. 5.83, 5.76, 5.37, and 5.27, respectively (Figure 5d). The gradual decrease in coordination numbers during discharge, with the distance of second-neighbor Ti–S increasing, results from the ratio of cations (Ti and Mg) and anions (S) varying significantly from 1:3 to 1.625:3. The first-neighbor S–S numbers decrease from 0.67 to 0.26 (Figures 5e and S28), signifying that covalent S–S bonds dissociate during the discharging process. Also, the distance of the first and second-neighbor S–S stretches with Mg<sup>2+</sup> insertion. Upon the magnesian process, the number of pairs for S–Mg (Figure 5f) and Ti–Mg (Figure S29) increases, while that for Ti–Ti (Figure S30) and Mg–S (Figure S31) decreases with Mg–Ti (Figure S32) remaining steady. Local structure models of a-TiS<sub>3</sub> (Figure 5g) and a-Mg<sub>0.625</sub>TiS<sub>3</sub> (Figure 5h) indicate that the discharging process induces structural changes, mainly embodied in the dissociation of the S–S bonds and a decrease in the coordination number of Ti.

As discussed above, both the discharge and charge curves of a-TiS<sub>3</sub> exhibit a single voltage plateau, corresponding to a gradual structure change of the amorphous host. The formation of conversion products such as Ti and MgS is not observed in the XRD, TEM, and Raman spectra in the discharged state (a-Mg<sub>0.625</sub>TiS<sub>3</sub>), due to the nucleation of MgS being suppressed by the amorphous structure. XPS and EELS spectra demonstrate that both cationic Ti and anionic S take part in the redox reaction. DFT-MD simulations indicate that the redox mechanism primarily involves two unique structural changes: (i) the dissociation/formation of S–S bonds and (ii) sharp changes in the coordination number of Ti. These two structural changes proceed continuously and in concert with Mg insertion/extraction, resulting in a unique mixture of intercalation and conversion reaction (MICR). Accordingly, the redox reaction of the a-TiS<sub>3</sub> sample can be proposed as follows:



## CONCLUSION

In this paper, we proposed an amorphization and anion enrichment strategy to mitigate the sluggish reaction kinetics and low-capacity delivery for Mg-ion cathodes by enhancing the solid-state ion diffusion, providing more ion-storage sites, and contributing to the local transfer of multiple electrons through the additional anionic redox centers. Accordingly, we designed a series of amorphous titanium polysulfides (TiS<sub>*x*</sub>, *x* = 2, 3, and 4) as cathode materials for RMBs. The electrochemical performance of amorphous polysulfides outperforms that of their crystalline counterparts. The a-TiS<sub>3</sub> sample is highlighted to offer a highly competitive energy density, appreciable cycling stability, and fast reaction kinetics. The a-TiS<sub>*x*</sub> sample remains amorphous during cycling with both Ti and S taking part in the redox reaction, called joint cationic and anionic redox-rich chemistry. During the magnesian process, the structure change mainly involves the dissociation of S–S bonds and changes in the coordination number of Ti, namely, a mixture of conversion and intercalation reaction. Our proposed amorphization and redox-rich strategy might be generalized to other transition metals (V, Mo, Nb, etc.) and

anions (oxides, fluorides, selenides, etc.) to design advanced cathode materials for multivalent-ion batteries.

## ■ EXPERIMENTAL SECTION

### Material Synthesis

The a-TiS<sub>x</sub> ( $x = 2, 3,$  and  $4$ ) samples were prepared by a mechanochemical process. Crystalline TiS<sub>2</sub> (99.8%; Alfa) and sulfur (99.5%; Alfa) with appropriate atomic ratios were weighed and mixed in an Ar-filled glovebox. The mixtures are sealed into a leak-proof jar filled with Ar gas. During ball milling, no air can infiltrate the jar, which will protect the mixture from oxidation by oxygen. A zirconia pot (45 mL) with zirconia balls (4 mm in diameter) was used, and the rotation speed of a planetary ball mill apparatus (P-7, Fritsch) was fixed at 800 rpm. After 48 h of ball-milling, a-TiS<sub>x</sub> samples were obtained.

c-TiS<sub>3</sub> samples were prepared by a solid-state reaction.<sup>20</sup> Specifically, Ti and S powders with a molar ratio of 1:3 were mixed with 5% excess of S. The mixture was sealed in a vacuum quartz tube and then heated to 500 °C at 2 °C/min and maintained for 72 h. After natural cooling to room temperature, the c-TiS<sub>3</sub> powder was obtained.

### Material Characterizations

The XRD patterns were measured using Cu K $\alpha$  radiation on an X'Pert Pro MPD X-ray diffractometer from 10° to 80° ( $2\theta$ ). The morphologies of samples were investigated by scanning electron microscopy (Hitachi S-4800), transmission electron microscopy (JEM 2100Plus, JEOL Limited Corporation, Japan), and advanced spherical aberration-corrected scanning transmission electron microscopy combined with high-angle annular dark field as well as annular bright field (JEM-ARM200CF, JEOL, Tokyo, Japan). The chemical composition was investigated by energy-dispersive spectroscopy (EDS). The atomic ratios of Ti and S for the obtained a-TiS<sub>x</sub> samples were analyzed by using an Agilent 7800 ICP-MS instrument. The X-ray photoelectron spectroscopy (XPS) spectra were recorded with a spectrometer having Mg/Al K $\alpha$  radiation (ESCALAB 250 Xi, Thermo Fisher). All binding energies reported were corrected using the signal of carbon at 284.8 eV as an internal standard. For ex situ XPS and EELS measurements, pouch cells with different conditions were disassembled in an argon-filled glovebox and the electrodes were washed in tetrahydrofuran (anhydrous, Alfa Aesar, 99.9%) three times to remove the electrolyte, and then the drying samples were obtained and moved to the machine with an argon-filled sealing tube as a transfer box. In this process, all samples were exposed to air within 3–4 s. The electrical conductivity measurement of electrodes is performed using a four-pin probe (Kyowa Electronic Instruments Co., Ltd., Japan) according to MCP-PD51.

### Electrochemical Measurements

Cell assembly was carried out in an Ar-filled glovebox with O<sub>2</sub> and H<sub>2</sub>O levels below 0.1 ppm. a-TiS<sub>x</sub> electrodes were prepared by compressing the as-prepared powders, ketjen black, PTFE at a weight ratio of 7:2:1 onto the molybdenum grid. The loading mass of electrodes is  $\sim 2$  mg/cm<sup>2</sup>. Rechargeable Mg batteries (RMBs) were assembled using pouch cells with MACC as the electrolyte, polished Mg metal as the anode, and Whatman glass fibers as separators. The electrochemical test was conducted on a LAND-CT2001A battery test station (LAND Electronic Co.) with a voltage cutoff of 0.5–2.5 V at room temperature. During GITT measurement, the electrode was discharged/charged at a pulse current of 20 mA/g for 1 h duration followed by 2 h relaxation at open circuit to reach equilibrium potentials. Nyquist plots were recorded using Autolab PGSTAT302N (Metrohm, Switzerland) at a frequency range of 0.01–100 kHz. The capacity throughout the paper is calculated based on the mass of a-TiS<sub>x</sub> samples.

### DFT-MD Simulations

Ab initio molecular dynamics (MD) simulations were performed using CP2K code.<sup>35</sup> The MD simulations were performed under the NVT ensemble. We used the DZVP-MOLOPT-SR-GTH basis set<sup>36</sup>

accompanying Goedecker–Teter–Hutter (GTH) pseudopotentials.<sup>37</sup> The complementary plane wave basis set had a cutoff of 700 Ry. The exchange-correlation functional used was GGA-PBE. The atomic partial charges were calculated by the restrained electrostatic potential (RESP) method.<sup>38</sup> The “melt-and-quake” approach was performed following an approach similar to that in ref 39. Amorphous a-TiS<sub>3</sub>, a-Mg<sub>0.25</sub>TiS<sub>3</sub>, a-Mg<sub>0.5</sub>TiS<sub>3</sub>, and a-Mg<sub>0.625</sub>TiS<sub>3</sub>, with 40, 34, and 36 atoms respectively, were equilibrated at 2000 K for 7000 steps. Then the temperature was decreased slowly to 300 K for 7000 steps. The cell size was determined by searching the cell size with minimum energy. Next the “melt-and-quake” approach was repeated for a  $2 \times 2 \times 2$  supercell for amorphous a-TiS<sub>3</sub>, a-Mg<sub>0.25</sub>TiS<sub>3</sub>, a-Mg<sub>0.5</sub>TiS<sub>3</sub>, and a-Mg<sub>0.625</sub>TiS<sub>3</sub>, with 40, 34, and 36 atoms. A time step of 1.2 fs was used for all MD simulations.

## ■ ASSOCIATED CONTENT

### Supporting Information

The Supporting Information is available free of charge at <https://pubs.acs.org/doi/10.1021/jacsau.1c00144>.

Experimental section, characterizations, electrochemical testing of a-TiS<sub>x</sub> samples, tables, and DFT-MD data (PDF)

## ■ AUTHOR INFORMATION

### Corresponding Author

**Liumin Suo** – Beijing Advanced Innovation Center for Materials Genome Engineering, Key Laboratory for Renewable Energy, Beijing Key Laboratory for New Energy Materials and Devices, Institute of Physics, Chinese Academy of Sciences, Beijing 100190, China; Center of Materials Science and Optoelectronics Engineering, University of Chinese Academy of Sciences, Beijing 100049, China; Yangtze River Delta Physics Research Center Co. Ltd., Liyang, Jiangsu 213300, China; [orcid.org/0000-0002-6772-8421](https://orcid.org/0000-0002-6772-8421); Email: [suoliumin@iphy.ac.cn](mailto:suoliumin@iphy.ac.cn)

### Authors

**Minglei Mao** – Beijing Advanced Innovation Center for Materials Genome Engineering, Key Laboratory for Renewable Energy, Beijing Key Laboratory for New Energy Materials and Devices, Institute of Physics, Chinese Academy of Sciences, Beijing 100190, China; Center of Materials Science and Optoelectronics Engineering, University of Chinese Academy of Sciences, Beijing 100049, China; [orcid.org/0000-0002-7628-4922](https://orcid.org/0000-0002-7628-4922)

**Chenxing Yang** – School of Physics and Astronomy, Shanghai Jiao Tong University, Shanghai 200240, China

**Zejing Lin** – Beijing Advanced Innovation Center for Materials Genome Engineering, Key Laboratory for Renewable Energy, Beijing Key Laboratory for New Energy Materials and Devices, Institute of Physics, Chinese Academy of Sciences, Beijing 100190, China

**Yuxin Tong** – Beijing Advanced Innovation Center for Materials Genome Engineering, Key Laboratory for Renewable Energy, Beijing Key Laboratory for New Energy Materials and Devices, Institute of Physics, Chinese Academy of Sciences, Beijing 100190, China

**Qinghua Zhang** – Beijing Advanced Innovation Center for Materials Genome Engineering, Key Laboratory for Renewable Energy, Beijing Key Laboratory for New Energy Materials and Devices, Institute of Physics, Chinese Academy of Sciences, Beijing 100190, China

**Lin Gu** – Beijing Advanced Innovation Center for Materials Genome Engineering, Key Laboratory for Renewable Energy, Beijing Key Laboratory for New Energy Materials and Devices, Institute of Physics, Chinese Academy of Sciences, Beijing 100190, China; [orcid.org/0000-0002-7504-031X](https://orcid.org/0000-0002-7504-031X)

**Liang Hong** – School of Physics and Astronomy, Shanghai Jiao Tong University, Shanghai 200240, China

**Yong-Sheng Hu** – Beijing Advanced Innovation Center for Materials Genome Engineering, Key Laboratory for Renewable Energy, Beijing Key Laboratory for New Energy Materials and Devices, Institute of Physics, Chinese Academy of Sciences, Beijing 100190, China; [orcid.org/0000-0002-8430-6474](https://orcid.org/0000-0002-8430-6474)

**Hong Li** – Beijing Advanced Innovation Center for Materials Genome Engineering, Key Laboratory for Renewable Energy, Beijing Key Laboratory for New Energy Materials and Devices, Institute of Physics, Chinese Academy of Sciences, Beijing 100190, China; [orcid.org/0000-0002-8659-086X](https://orcid.org/0000-0002-8659-086X)

**Xuejie Huang** – Beijing Advanced Innovation Center for Materials Genome Engineering, Key Laboratory for Renewable Energy, Beijing Key Laboratory for New Energy Materials and Devices, Institute of Physics, Chinese Academy of Sciences, Beijing 100190, China

**Liquan Chen** – Beijing Advanced Innovation Center for Materials Genome Engineering, Key Laboratory for Renewable Energy, Beijing Key Laboratory for New Energy Materials and Devices, Institute of Physics, Chinese Academy of Sciences, Beijing 100190, China

Complete contact information is available at:  
<https://pubs.acs.org/10.1021/jacsau.1c00144>

## Notes

The authors declare no competing financial interest.

## ACKNOWLEDGMENTS

This work was supported by the National Natural Science Foundation of China (21905299) and the Center for Clean Energy. Minglei Mao acknowledges the China Postdoctoral Science Foundation (2019TQ0346, 2020M670508).

## REFERENCES

- (1) Yoo, H. D.; Shterenberg, I.; Gofar, Y.; Gershinsky, G.; Pour, N.; Aurbach, D. Mg rechargeable batteries: an on-going challenge. *Energy Environ. Sci.* **2013**, *6*, 2265–2279.
- (2) Mao, M.; Gao, T.; Hou, S.; Wang, C. A critical review of cathodes for rechargeable Mg batteries. *Chem. Soc. Rev.* **2018**, *47*, 8804–8841.
- (3) Liang, Y.; Dong, H.; Aurbach, D.; Yao, Y. Current status and future directions of multivalent metal-ion batteries. *Nature Energy* **2020**, *5*, 646–656.
- (4) Mao, M.; Ji, X.; Hou, S.; Gao, T.; Wang, F.; Chen, L.; Fan, X.; Chen, J.; Ma, J.; Wang, C. Tuning Anionic Chemistry To Improve Kinetics of Mg Intercalation. *Chem. Mater.* **2019**, *31*, 3183–3191.
- (5) Gershinsky, G.; Yoo, H. D.; Gofar, Y.; Aurbach, D. Electrochemical and Spectroscopic Analysis of Mg<sup>2+</sup> Intercalation into Thin Film Electrodes of Layered Oxides: V<sub>2</sub>O<sub>5</sub> and MoO<sub>3</sub>. *Langmuir* **2013**, *29*, 10964–10972.
- (6) Incorvati, J. T.; Wan, L. F.; Key, B.; Zhou, D.; Liao, C.; Fuoco, L.; Holland, M.; Wang, H.; Prendergast, D.; Poepplmeier, K. R.; Vaughn, J. T. Reversible Magnesium Intercalation into a Layered Oxyfluoride Cathode. *Chem. Mater.* **2016**, *28*, 17–20.
- (7) Zhang, R.; Ling, C. Unveil the Chemistry of Olivine FePO<sub>4</sub> as Magnesium Battery Cathode. *ACS Appl. Mater. Interfaces* **2016**, *8*, 18018–18026.
- (8) Arthur, T. S.; Zhang, R.; Ling, C.; Glans, P.-A.; Fan, X.; Guo, J.; Mizuno, F. Understanding the Electrochemical Mechanism of K- $\alpha$ MnO<sub>2</sub> for Magnesium Battery Cathodes. *ACS Appl. Mater. Interfaces* **2014**, *6*, 7004–7008.
- (9) Mao, M.; Lin, Z.; Tong, Y.; Yue, J.; Zhao, C.; Lu, J.; Zhang, Q.; Gu, L.; Suo, L.; Hu, Y.-S.; Li, H.; Huang, X.; Chen, L. Iodine Vapor Transport-Triggered Preferential Growth of Chevrel Mo<sub>6</sub>S<sub>8</sub> Nano-sheets for Advanced Multivalent Batteries. *ACS Nano* **2020**, *14*, 1102–1110.
- (10) Sun, X.; Bonnick, P.; Duffort, V.; Liu, M.; Rong, Z.; Persson, K. A.; Ceder, G.; Nazar, L. F. A high capacity thiospinel cathode for Mg batteries. *Energy Environ. Sci.* **2016**, *9*, 2273–2277.
- (11) Sun, X.; Bonnick, P.; Nazar, L. F. Layered TiS<sub>2</sub> Positive Electrode for Mg Batteries. *ACS Energy Lett.* **2016**, *1*, 297–301.
- (12) Bonnick, P.; Blanc, L.; Vajargah, S. H.; Lee, C.-W.; Sun, X.; Balasubramanian, M.; Nazar, L. F. Insights into Mg<sup>2+</sup> Intercalation in a Zero-Strain Material: Thiospinel Mg<sub>x</sub>Zr<sub>2</sub>S<sub>4</sub>. *Chem. Mater.* **2018**, *30*, 4683–4693.
- (13) Liu, M.; Rong, Z.; Malik, R.; Canepa, P.; Jain, A.; Ceder, G.; Persson, K. A. Spinel compounds as multivalent battery cathodes: a systematic evaluation based on ab initio calculations. *Energy Environ. Sci.* **2015**, *8*, 964–974.
- (14) Machida, N.; Fuchida, R.; Minami, T. Behavior of Rapidly Quenched V<sub>2</sub>O<sub>5</sub> Glass at Cathode in Lithium Cells. *J. Electrochem. Soc.* **1989**, *136*, 2133–2136.
- (15) Arthur, T. S.; Kato, K.; Germain, J.; Guo, J.; Glans, P.-A.; Liu, Y.-S.; Holmes, D.; Fan, X.; Mizuno, F. Amorphous V<sub>2</sub>O<sub>5</sub>-P<sub>2</sub>O<sub>5</sub> as high-voltage cathodes for magnesium batteries. *Chem. Commun.* **2015**, *51*, 15657–15660.
- (16) Hayashi, A.; Matsuyama, T.; Sakuda, A.; Tatsumisago, M. Amorphous Titanium Sulfide Electrode for All-solid-state Rechargeable Lithium Batteries with High Capacity. *Chem. Lett.* **2012**, *41*, 886–888.
- (17) Sakuda, A.; Taguchi, N.; Takeuchi, T.; Kobayashi, H.; Sakaebe, H.; Tatsumi, K.; Ogumi, Z. Amorphous TiS<sub>4</sub> positive electrode for lithium-sulfur secondary batteries. *Electrochem. Commun.* **2013**, *31*, 71–75.
- (18) Sakuda, A.; Taguchi, N.; Takeuchi, T.; Kobayashi, H.; Sakaebe, H.; Tatsumi, K.; Ogumi, Z. Amorphous Niobium Sulfides as Novel Positive-Electrode Materials. *ECS Electrochem. Lett.* **2014**, *3*, A79–A81.
- (19) Mao, M.; Tong, Y.; Zhang, Q.; Hu, Y.-S.; Li, H.; Huang, X.; Chen, L.; Gu, L.; Suo, L. Joint Cationic and Anionic Redox Chemistry for Advanced Mg Batteries. *Nano Lett.* **2020**, *20*, 6852–6858.
- (20) Taniguchi, K.; Gu, Y.; Katsura, Y.; Yoshino, T.; Takagi, H. Rechargeable Mg battery cathode TiS<sub>3</sub> with d-p orbital hybridized electronic structures. *Appl. Phys. Express* **2016**, *9*, 011801.
- (21) Grayfer, E. D.; Pazhetnov, E. M.; Kozlova, M. N.; Artemkina, S. B.; Fedorov, V. E. Anionic Redox Chemistry in Polysulfide Electrode Materials for Rechargeable Batteries. *ChemSusChem* **2017**, *10*, 4805–4811.
- (22) Osticioli, I.; Zoppi, A.; Castellucci, E. M. Shift-Excitation Raman Difference Spectroscopy—Difference Deconvolution Method for the Luminescence Background Rejection from Raman Spectra of Solid Samples. *Appl. Spectrosc.* **2007**, *61*, 839–844.
- (23) Glebko, N.; Aleksandrova, I.; Tewari, G. C.; Tripathi, T. S.; Karppinen, M.; Karttunen, A. J. Electronic and Vibrational Properties of TiS<sub>2</sub>, ZrS<sub>2</sub>, and HfS<sub>2</sub>: Periodic Trends Studied by Dispersion-Corrected Hybrid Density Functional Methods. *J. Phys. Chem. C* **2018**, *122*, 26835–26844.
- (24) Zhang, S. S. The redox mechanism of FeS<sub>2</sub> in non-aqueous electrolytes for lithium and sodium batteries. *J. Mater. Chem. A* **2015**, *3*, 7689–7694.
- (25) Wen, C. J.; Boukamp, B. A.; Huggins, R. A.; Weppner, W. Thermodynamic and Mass Transport Properties of “LiAl. *J. Electrochem. Soc.* **1979**, *126*, 2258–2266.

(26) Mao, M.; Gao, T.; Hou, S.; Wang, F.; Chen, J.; Wei, Z.; Fan, X.; Ji, X.; Ma, J.; Wang, C. High-Energy-Density Rechargeable Mg Battery Enabled by a Displacement Reaction. *Nano Lett.* **2019**, *19*, 6665–6672.

(27) Zhu, Y.; Gao, T.; Fan, X.; Han, F.; Wang, C. Electrochemical Techniques for Intercalation Electrode Materials in Rechargeable Batteries. *Acc. Chem. Res.* **2017**, *50*, 1022–1031.

(28) Weber, T.; Muijsers, J. C.; Niemantsverdriet, J. W. Structure of Amorphous MoS<sub>3</sub>. *J. Phys. Chem.* **1995**, *99*, 9194–9200.

(29) Hibble, S. J.; Walton, R. I.; Pickup, D. M.; Hannon, A. C. Amorphous MoS<sub>3</sub>: clusters or chains? The structural evidence. *J. Non-Cryst. Solids* **1998**, *232–234*, 434–439.

(30) Fleet, M. E.; Harmer, S. L.; Liu, X.; Nesbitt, H. W. Polarized X-ray absorption spectroscopy and XPS of TiS<sub>3</sub>: S K- and Ti L-edge XANES and S and Ti 2p XPS. *Surf. Sci.* **2005**, *584*, 133–145.

(31) Matsuyama, T.; Deguchi, M.; Mitsuhara, K.; Ohta, T.; Mori, T.; Orikasa, Y.; Uchimoto, Y.; Kowada, Y.; Hayashi, A.; Tatsumisago, M. Structure analyses using X-ray photoelectron spectroscopy and X-ray absorption near edge structure for amorphous MS<sub>3</sub> (M: Ti, Mo) electrodes in all-solid-state lithium batteries. *J. Power Sources* **2016**, *313*, 104–111.

(32) Sun, G.; Wei, Z.; Chen, N.; Chen, G.; Wang, C.; Du, F. Quasi-1D TiS<sub>3</sub>: A potential anode for high-performance sodium-ion storage. *Chem. Eng. J.* **2020**, *388*, 124305.

(33) Mao, M.; Mei, L.; Guo, D.; Wu, L.; Zhang, D.; Li, Q.; Wang, T. High electrochemical performance based on the TiO<sub>2</sub> nanobelt@few-layered MoS<sub>2</sub> structure for lithium-ion batteries. *Nanoscale* **2014**, *6*, 12350–12353.

(34) Mao, M.; Yan, F.; Cui, C.; Ma, J.; Zhang, M.; Wang, T.; Wang, C. Pipe-Wire TiO<sub>2</sub>-Sn@Carbon Nanofibers Paper Anodes for Lithium and Sodium Ion Batteries. *Nano Lett.* **2017**, *17*, 3830–3836.

(35) Hutter, J.; Iannuzzi, M.; Schiffmann, F.; VandeVondele, J. cp2k: atomistic simulations of condensed matter systems. *WIREs Comput. Mol. Sci.* **2014**, *4*, 15–25.

(36) VandeVondele, J.; Hutter, J. Gaussian basis sets for accurate calculations on molecular systems in gas and condensed phases. *J. Chem. Phys.* **2007**, *127*, 114105.

(37) Krack, M. Pseudopotentials for H to Kr optimized for gradient-corrected exchange-correlation functionals. *Theor. Chem. Acc.* **2005**, *114*, 145–152.

(38) Bayly, C. I.; Cieplak, P.; Cornell, W.; Kollman, P. A. A well-behaved electrostatic potential based method using charge restraints for deriving atomic charges: the RESP model. *J. Phys. Chem.* **1993**, *97*, 10269–10280.

(39) Sakuda, A.; Ohara, K.; Fukuda, K.; Nakanishi, K.; Kawaguchi, T.; Arai, H.; Uchimoto, Y.; Ohta, T.; Matsubara, E.; Ogumi, Z.; Okumura, T.; Kobayashi, H.; Kageyama, H.; Shikano, M.; Sakaebe, H.; Takeuchi, T. Amorphous Metal Polysulfides: Electrode Materials with Unique Insertion/Extraction Reactions. *J. Am. Chem. Soc.* **2017**, *139*, 8796–8799.